CHINA FOUNDRY Research & Development
Vol. 21 No. 3 May 2024
www.springer.com/41230
https://doi.org/10.1007/s41230-024-3049-2

Assessing efficacy of standard impregnation techniques on die-cast aluminum alloys using X-ray micro-CT

***Ajith Bandara[1], Koichi Kan[1], Katanaga Yusuke[1, 2], Natsuto Soga[1, 2], Akifumi Koike[3], and Toru Aoki[2, 3, 4]**

1. Hamamatsu TSC, Chuo Hatsumei Institute, 322 lida-cho, Minami-ku, Hamamatsu, 435-0028, Japan

2. Graduate School of Medical Photonics, ShizuokaUniversity, Johoku 3-5-1, Hamamatsu, Shizuoka, 432-8561, Japan

3. ANSeeN Inc, Johoku 3-5-1, Hamamatsu, Shizuoka, 432-8561, Japan

4. Research Institute of Electronics, ShizuokaUniversity, Johoku 3-5-1, Hamamatsu, Shizuoka, 432-8561, Japan

Abstract: Utilizing lightweight Al alloys in various industrial applications requires achieving precise pressure tightness and leak requirements. Vacuum pressure impregnation (VPI) with thermosetting polymers is commonly used to address leakage defects in die-cast Al alloys. In this study, the efficacy of the VPI technique in sealing alloy parts was investigated using a combination of nondestructive micro X-ray computed tomography (micro XCT) and a standard leak test. The results demonstrate that the commonly used water leak test is insufficient for determining the sealing performance. Instead, micro XCT shows distinct advantages by enabling more comprehensive analysis. It reveals the presence of a low atomic number impregnates sealant within casting defects, which has low grey contrast and allows for visualizing primary leakage paths in 3D. The effective atomic number of impregnated resin is 6.75 and that of Al alloy is 13.69 by dual-energy X-ray CT. This research findings will contribute to enhancing the standard VPI process parameters and the properties of impregnating sealants to improve quality assurance for impregnation in industrial metals.

Keywords: nondestructive testing; Al alloy die-casting; vacuum pressure impregnation; micro X-ray computed tomography; duel-energy X-ray CT

CLC numbers: TG146.21 **Document code:** A **Article ID:** 1672-6421(2024)03-276-11

1 Introduction

Die-casting has become widely adopted for producing industrial parts with complex shapes and geometries. The use of lightweight metals, such as aluminum, magnesium, beryllium, and titanium alloys, has grown in popularity in the automotive industry owing to their numerous benefits, including reduced weight, improved fuel efficiency, lower oil consumption, reduced emissions, and improved resistance to corrosion, excellent ductility and strength [1-6]. High-pressure die-casting (HPDC) is the primary method for producing around 60% of the light-alloy castings in the automotive sector [7]. Although HPDC offers fast and efficient production, it can result in 5%–10% scrap due to challenging defects like hydrogen gas pores, shrinkage porosity, misruns, and cold shuts. The causes and mechanisms behind these defects have been well studied and documented [8-14].

In some instances, pores in Al alloy parts can be accepted based on their size, shape, and location, with criteria determined by supplier specifications and testing [15]. However, these defects can negatively impact the casting's mechanical properties, corrosion resistance, and air tightness, reducing performance and reliability [16]. Interconnected pores and leakage paths are typical in light alloy die-casting and often result in the leaking of gases, liquids, and oil, making the castings unsuitable for many applications. Efforts have been made to minimize gas and shrink pores through process optimization to minimize the risk of product failure and scrap rate during production [17-22]. Vacuum and ultra-vacuum die-casting processes are

***Ajith Bandara**

Ph. D., Researcher. Research interests: Industrial X-ray computed tomography, material science, metallurgy, machine learning, optoelectronics, and nanostructure science.

E-mail: chuhatsu.gkc1@gmail.com

Received: 2023-05-21; Accepted: 2024-03-15

superior to HPDC in reducing porosity, minimizing blisters, improving surface finish, and enhancing mechanical and dynamic properties [23-31]. Despite advancements in casting technology, the complete elimination of pores remains a significant challenge. Thus, impregnation treatments are employed to reduce such vulnerabilities and to mitigate the risk of product failure due to leakage and porosity. The vacuum pressure impregnation (VPI) technique offers a cost-effective solution for sealing pores and eliminating leakage paths, assuring the quality of cast components [32-35]. This process is more affordable than scrapping parts, giving manufacturers a high degree of confidence in the quality of the impregnated components. However, to ensure that the VPI process has been implemented effectively, it is essential to conduct a thorough evaluation using appropriate testing methods.

The efficacy of impregnation is currently assessed using the dipping water leak test, following the guidelines of Military standard MIL-STD-276A [35, 36]. The process seals porous alloy castings and powder metal components, evaluating the efficacy of sealing through pre- and post-impregnation testing. Leakage absence is crucial for VPI's success. However, the dipping water leak test has limitations. It cannot ascertain crucial details, such as whether the resin material has wholly sealed the leakage or only partially filled the leakage paths.

Additionally, leakage paths can have complex structures undetectable by the leak test alone. Ensuring the reliability and life of lightweight alloy parts requires a more certain assessment of impregnation efficacy. Additional methods like microscopic analysis or nondestructive testing (NDT) are necessary to understand resin distribution and identify potential issues. Hence, this study introduced a novel application of laboratory-based semi-automated micro X-ray computed tomography (micro XCT), utilizing advanced direct conversion pixel-Pt/CdTe/In flat panel detectors (FPDs) for both qualitative and quantitative analysis of impregnation technique in sealing die-casting defects of industrial Al alloy (A383) samples. Micro XCT is an NDT method widely used for analyzing metal alloy defects [37-44]. However, there is limited research on using XCT to visualize and characterize impregnation resin for sealing casting defects. The low atomic number and mass density of the resin cause reduced X-ray attenuation [45], making it challenging to detect in CT images due to the hardening of the X-ray beam and reduced attenuation by higher energy X-ray photons. The impregnation resin is typically localized within a narrow region of the casting defect, further complicating the acquisition of CT images with adequate contrast and spatial resolution.

Nevertheless, the methodology utilizing micro XCT and advanced FPDs proposed by our group proves suitable for generating high-resolution 2D and 3D CT images, facilitating the accurate characterization and evaluation of internal defects and the impregnation efficacy nondestructively. The implementation of these lightweight, portable, and compact FPDs offers several advantages, including higher X-ray conversion efficiency compared to scintillating materials, 100% conversion energy signal, the ability to measure X-ray energy through photon counting, optical diffusion-free imaging, high-speed processing with LSI, and gapless tiling. Unlike traditional methods that often require several hours for quality projection data acquisition and detailed analysis, FPDs combined with the CT reconstruction software enable the generation of high-resolution CT images with detailed analysis within several minutes.

This study finding maybe highlight the limitations of using the leak test for assessing the efficacy of the impregnation process and determining pore size. Water leak test was conducted using three A383 samples. 3D CT imaging was employed to gain comprehensive insight into the internal structure of the Al alloys, to expose intricate details of the casting defects, including dimensional and geometrical characteristics. Notably, the findings challenged the conventional assumption of uniformity in leakage paths, revealing their irregular nature. Utilizing 2D CT slice images, we successfully identified the impregnated resin material within the casting defects by providing the sealed conditions of the leakage paths in Al alloys.

Moreover, the implementation of a dual-energy X-ray CT (DXCT) technique [46, 47] with a CdTe photon counting detector accurately differentiated the impregnation resin and Al alloy based on their effective atomic numbers (EANs). The analysis confirmed the presence of the commercially used P601 resin within the defects in the casing. The micro XCT approach simplifies sample preparation, handling, and data processing, allowing a comprehensive evaluation of the impregnation process's efficacy without compromising structural integrity. Hence, this study's findings are anticipated to significantly enhance the process parameters of the impregnation technique and improve the properties of the sealing resin utilized for sealing casting defects in industrial alloys.

2 Experimental section

2.1 Samples and leak test

Three standard Al alloy (A383, ρ=2.74 g·cm^{-3}) samples that met ISO 17615 standards were utilized. The samples were uniform in shape, with a thickness of 5 mm and a diameter of 6 cm. The HPDC technique was employed to produce the alloy samples, with the in-gate speed at 50 m·s^{-1} and die cavity pressures of up to 120 MPa (Mikawa Koki Fukuroi Manufacturing Co., Ltd., Japan).

A standard water leak test was performed on all the Al alloy samples before and after the VPI. The identified significant leakage in the samples was indicated with circles, as illustrated in Fig. 1.

The leak test procedure involved submerging and securely fastening each alloy sample, followed by applying pressurized air from the bottom. The significant leakage was inspected, and severity was determined by measuring the leak rate. The collection of air bubbles from significant leakage was carried out using a measuring cylinder. The leak rate was then calculated by measuring the air volume at various time

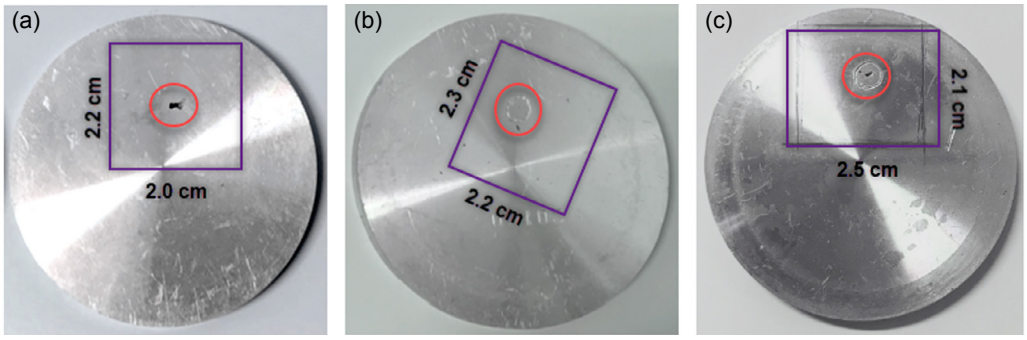

Fig. 1: Images of die-cast Al alloy test pieces: (a) Sample 1; (b) Sample 2; (c) Sample 3

intervals for Samples 2 and 3. However, due to an exceedingly high level of leakage in Sample 1, the leak rate during the experiment was not calculated.

The diameter of the primary leakage paths was estimated by applying Hagen-Poiseuille's law, as shown in Eq. (1). The calculated leak rates and corresponding diameters are reported in Table 1. The leakage path diameter is approximated based on the assumption of a uniform and straight pathway [48]. The diameter value represents the most constricted point in the leakage pathway.

$$Q=(\pi \cdot D^4 \cdot \Delta P)/128 \cdot \mu \cdot L \quad (1)$$

where, Q is the amount of leak measured in mL·min^{-1}, D is the diameter of the leakage path, ΔP is the pressure difference across the alloys sample (0.49 MPa), μ is the air viscosity, and L is the pore length. The pore length was considered 5 mm, the same as the sample's thickness.

Table 1: Classification of leakage path based on the leak test

Sample	Leak rate (mL·min^{-1})	Leak path diameter (mm)	Classification of leak	Leak status after the impregnation
1	–	–	Much leak	Leaking
2	1.28	0.02	Little leak	Not leaking
3	20.41	0.04	Medium leak	Not leaking

2.2 Vacuum pressure impregnation

A standard VPI treatment was used as specified in MIL-STD-276A Method B. After the pre-leak test, the three Al alloy samples were placed inside a vacuum autoclave for the impregnation. The autoclave was then evacuated to a pressure of 65 Pa for 5 min to eliminate any trapped air, moisture, or other residual substances present within the micropores of the samples. Next, a thermoset polymer sealant [(Super Sealant P601 (1.06 g·cm^{-3})] based on hydroxyl ethyl methacrylate monomers was introduced into the chamber as the impregnating resin (Chuo Hatsumei Institute Co., Ltd., Japan). The vacuum level was maintained while the resin was introduced, and the process was carried out for 15 min. After the sealant was loaded, the vacuum was released, and a positive pressure of 0.4 MPa was applied to force the resin into the casting defects. The pressure was then released, and any excess resin was drained away. The samples were thoroughly washed to remove any residual impregnate sealant from the surfaces. The goal was to ensure the samples being free of excess sealant, leaving only the impregnated resin within the internal defects. The alloy samples were then placed in an oven and heated to approximately 95 ºC for 1 h to ensure the hardening of the resin through cross-link polymerization. The entire impregnation treatment process is depicted in Fig. 2. The leak tightness test was re-executed on the impregnated samples to verify the efficacy of the VPI.

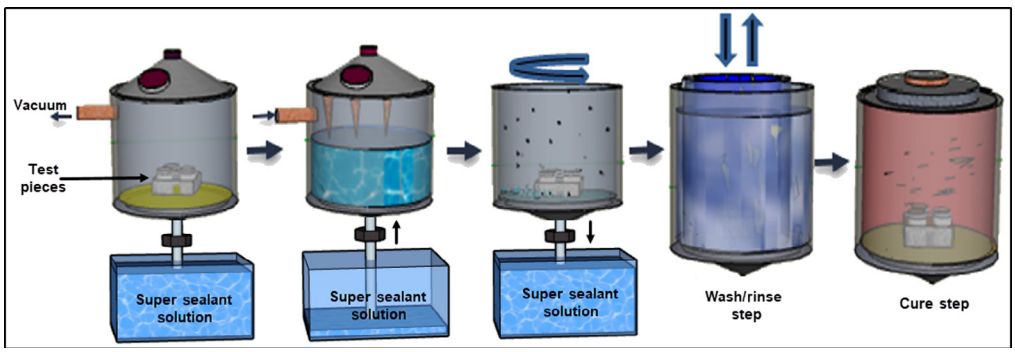

Fig. 2: Process diagram of the vacuum pressure impregnation

2.3 Characterization techniques

The NDT of defects and the evaluation of impregnation efficacy in the Al alloy samples were conducted using two methods. Firstly, a qualitative analysis was performed using a laboratory-based industrial microfocus XCT source (L12161-07) equipped with a state-of-the-art direct conversion Pt/CdTe/In-based X-ray flat-panel detector from ANSeeN Inc., Hamamatsu. Secondly, a DXCT quantitative analysis followed this was performed to identify the impregnating material, P601 resin, within the casting defects using a photon-counting XCounter detector from XC-Hydra-FX20 (Direct Conversion AB, Sweden).

2.3.1 Qualitative analysis

The projection data for each impregnated Al alloy sample were recorded using an X-ray FPD while rotating the sample's stage of the X-ray system at a speed of $4°{\cdot}s^{-1}$. Each sample's regions of interest (ROI) marked with rectangles in Fig. 1 were considered throughout the X-ray inspection. The FPD utilized in the experiment was a Schottky diode type with a pixel pitch of 100 μm and a pixel arrangement of 252 rows and 1,024 columns. The distance from X-ray source to detector was set to 500 mm, and the maximum geometrical magnification of the samples was achieved by positioning the sample stage of the system to a distance of 275 mm from the X-ray source. The focal spot size of the X-ray source was set to 50 μm, and the projection images were obtained using a cone-beam computed tomography (CBCT) geometry, as illustrated in Fig. 3. In the qualitative analysis, the primary goal is to thoroughly examine the entire volume of Al alloy metal samples and analyze internal casting defects. Therefore, the CBCT geometry was used in the micro XCT source. The CBCT configuration involves a conical or pyramid-shaped X-ray beam that diverges from the source, covering a wide area. Using the FPD with a resolution of 1,024×252 pixels, the complete sample volume's projection images were captured, ensuring sufficient magnification. This coverage allows detailed 3D reconstruction, revealing internal structure and defects in the Al alloy samples.

Before capturing the projection images of the Al alloy samples, the FPD was calibrated for five different X-ray voltages. The FPD recorded 2700 X-ray projection images, each with a pixel intensity split into 14-bit grey values, allowing for differentiation of over 16,000 intensity variations and transforming into greyscale values. The samples were rotated under an X-ray tube setting of 135 kV and 250 μA while the images were recorded. A 0.2 mm thick copper filter was utilized during imaging to prevent low X-ray energies and minimize beam-hardening artifacts. Subsequently, the 2D CT slices of each sample were reconstructed using acustom-developed CBCT software based on the filtered-back projection (FBP) method [49, 50]. The resulting slices were stacked to form comprehensive 3D CT images of the Al alloy samples for further internal structure analysis. The 2D and 3D CT images were further analyzed using Fiji and 3D slicer image processing software and their built-in filters [51, 52]. The ISO50 threshold was applied to distinguish between the Al alloys, impregnating resin, and air/pores within the sample images [53].

2.3.2 Quantitative analysis

The quantitative study of the impregnation material within the casting defects of the Sample 3 was conducted using the photon-counting XCounter detector, which features 131,072 high-resolution CdTe pixels arranged in 64 rows and 2,048 columns. Initially, we calibrated the XCounter against the background data using its built-in calibration function. Subsequently, the sample's X-ray attenuation data was captured across energy levels exceeding 30 keV, 50 keV, 70 keV, and 90 keV, utilizing a $4°{\cdot}s^{-1}$ stepwise rotation for 360° at 30 frames per second. The X-ray source-detector distance was set at 500 mm, while the X-ray source-sample distance was adjusted to 215 mm. A fan-beam geometry of the X-ray source was employed, as illustrated in Fig. 4, with an application of 150 kV and 200 μA X-ray tube settings to ensure the acquisition of high-quality images.

After that, the recorded X-ray attenuation data were utilized to generate two sets of CT images of 30–50 keV and 70–90 keV low and high-energy windows with the FBP method integrated into the CBCT software. The EANs of the impregnated resin material within the defects and Al alloys were computed based on their respective linear attenuation coefficients for the two energy windows, as the methodology outlined in Eq. (2) [54, 55]:

$$Z^4 = \frac{\mu(E_2)G(E_1,Z) - \mu(E_1)G(E_2,Z)}{\mu(E_1)F(E_2,Z) - \mu(E_2)F(E_1,Z)} \quad (2)$$

where, $\mu(E_1)$ and $\mu(E_2)$ are the linear attenuation coefficients for low and high-energy windows. $G(E_1, Z)$ and $G(E_2, Z)$ are the electron cross-section for the scattering term, and $F(E_1, Z)$ and $F(E_2, Z)$ represent the photoelectric effects in the low and high-energy windows, respectively.

The calculated EANs ($Z_{eff(exp)}$) were then compared to the theoretical EANs ($Z_{eff(th)}$) of the P601 sealant and the

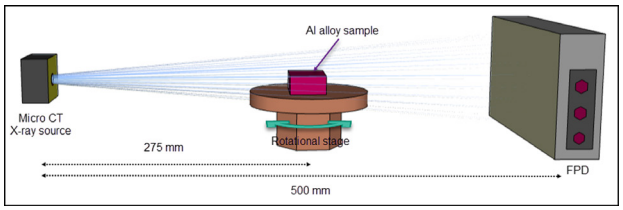

Fig. 3: Schematic diagram of the experimental CBCT setup with the FPD

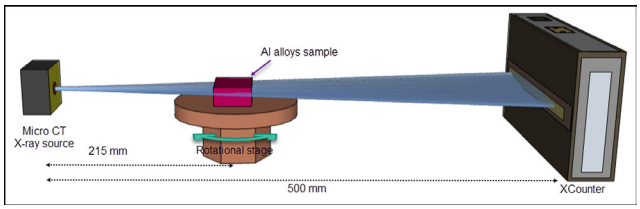

Fig. 4: Schematic diagram of the experimental FBCT setup with the XCounter

atomic number of aluminum. The theoretical EAN of the P601 sealant, which primarily comprises hydroxyl ethyl methacrylate, was calculated using the XMuDat method [56].

3 Results and discussion

3.1 Leak test and impregnation

Table 1 represents the calculated primary leakage path diameters of Samples 2 and 3 using the Hagen-Poiseuille equation. In the calculations for leakage diameters, it was assumed that the leakages formed during the die-casting process were uniform and straight. However, this assumption does not consider the intricate geometry of casting defects, which can result in variations in the calculated leakage diameters. The results of the VPI are also shown in Table 1. Samples 2 and 3 do not exhibit any leaking, but the central leakage path of Sample 1 is not effectively sealed by the impregnation process, as evidenced by the presence of air leaks.

It is important to note that the dipping water leak test results alone are insufficient to determine the efficacy of sealing process, even in Samples 2 and 3. The existence of open shrinkage cavities in the Al alloy casting samples, which cannot be detected through this test, highlights the need for a more comprehensive evaluation method to assess the airtightness performance of the impregnated casting defects.

3.2 Qualitative micro-CT analysis

CBCT was used for nondestructive imaging to evaluate the efficacy of the impregnation process in sealing the leakage paths in the Al alloy samples. The 3D CT images of the ROI in Sample 1 demonstrate the presence of a leakage path caused by die-casting, as depicted in Fig. 5. The top and side view 3D images provide a clearer understanding of the internal geometrical dimensions of the primary leakage. Contrary to the assumption made during the leak test, the leakage path was found to be neither uniform nor straight, and a significant crack is observed in the middle of the primary leaking defect.

In addition to the primary leakage path, tiny casting defect pores are also present. However, it is challenging to determine the impregnation resin status in these defects using 3D CT images. Further dimensional data analysis of the leakage path is presented in Fig. 6. The smallest leakage region has a diameter of approximately 0.68 mm. Furthermore, a 0.85 mm internal crack is also identified in Sample 1, as shown in Fig. 6(a). However, the diameter of the primary leakage during the leak test is assumed to be constant throughout the leaking hole. In contrast, a significant cavity of approximately 5.54 mm is observed in the middle of the leaking hole, as depicted in Fig. 6(b). This comparatively sizeable internal cavity may be attributed to the shrinkage of the molten Al alloy during the die-casting process.

The 2D CT slice image in Fig. 6(b) verifies the leak test results after the impregnation. The black highlights the presence of air in the leakage, indicating that the VPI treatment fails to seal the leakage path of Sample 1.

In Sample 2, a small leak is observed, but it shows no further leakage after the impregnation. The primary leaking regions are identified using 3D CT images, the position of the leakage can be seen in red circles in Fig. 7. The top and side

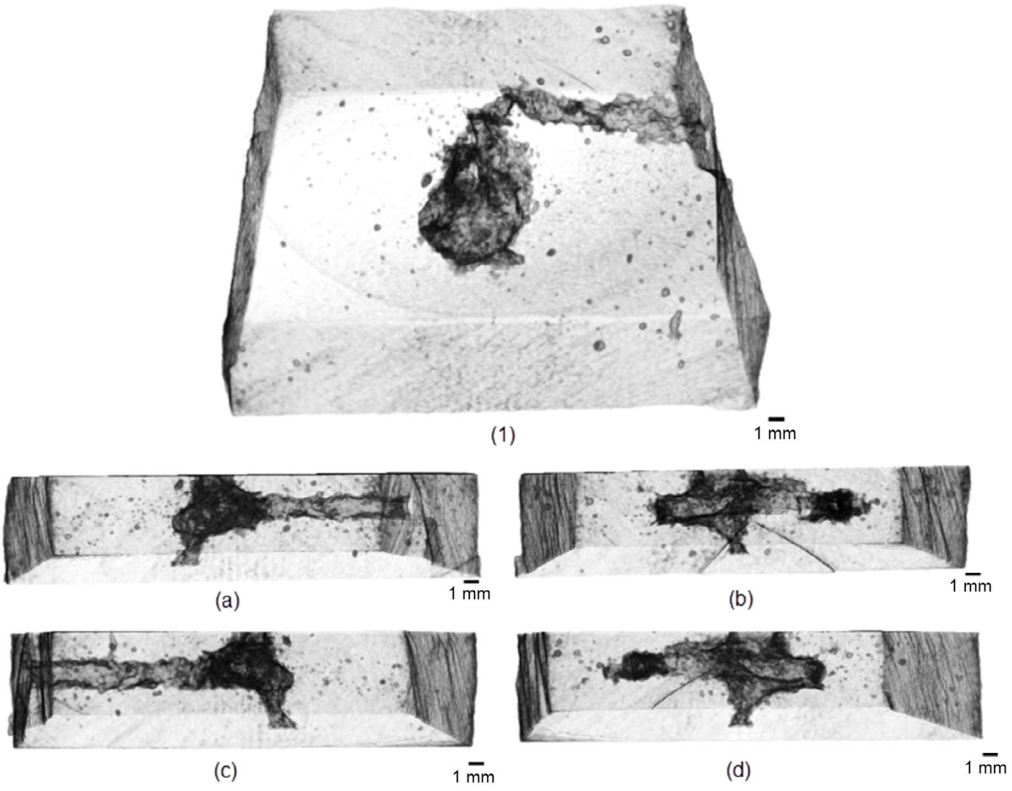

Fig. 5: 3D CT images of Sample 1: (1) normal view; (a), (b), (c), and (d) side views, respectively, by clock-wise rotation of the sample

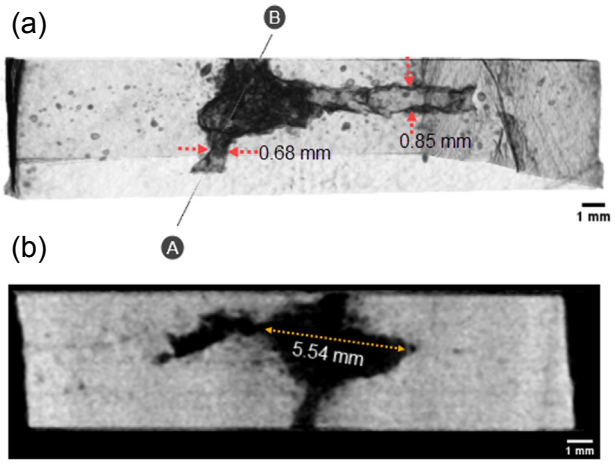

Fig. 6: CT images of Sample 1: (a) side-view 3D CT; (b) cross-sectional 2D CT slice image across the Line AB of 3D CT image

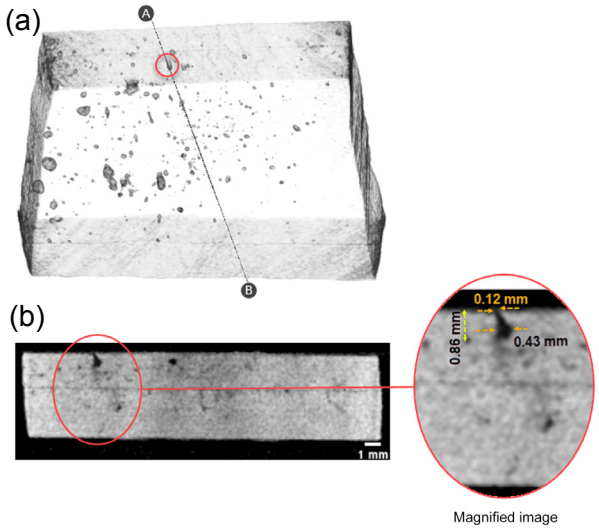

Fig. 8: CT images of Sample 2: (a) 3D CT image; (b) CT slice image across the Line AB

views of the images reveal internal casting pores with various sizes and a slight extension of the primary leakage path into the sample, as depicted in Fig. 7(b). However, to determine the presence of the impregnation sealant, a more in-depth analysis of cross-sectional 2D CT slice images of the leakage path is necessary. The starting of the leakage may not have contained the impregnation sealant, but the rest of the path may have been sealed effectively by the resin.

The contrast in the grey values of the 2D CT slice image across the primary leak path, as depicted in Fig. 8(b), suggests that the impregnating sealant is absent at the initiation of the leakage but is effective in sealing the rest of the defect. The unsealed cavity is found to be deep, with a depth of approximately 0.86 mm from the top surface of the sample. The width at the top is approximately 0.12 mm and increased by approximately 0.43 mm in the middle, as observed in the magnified image in Fig. 8(b). The leakage path becomes increasingly confined towards the center of the sample, with the smallest diameter reaching approximately 0.02 mm.

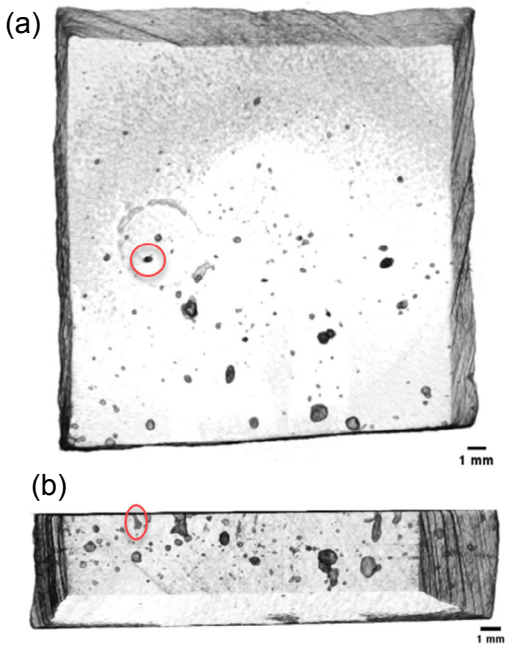

Fig. 7: 3D CT images of Sample 2: (a) top view; (b) side view

The incomplete sealing of the top part of the leakage in Sample 2 may have been caused by several factors. The curing process of the infiltrated liquid resin during the impregnation could have reduced the sealant in the broader part of the leakage due to condensation. The spinning and washing steps used in the impregnation may have also contributed to resin removal from the cavity. However, the impact of these steps is believed to be more significant in Sample 1, which has a comparatively larger leakage than Sample 2. This unsealed cavity, resulting from inadequate impregnation process parameters, may lead to potential failures in the future.

The occurrence of open shrinkage cavities in Al alloys during the die-casting process can negatively impact product quality if these defects are not adequately sealed by polymer resin during the impregnation process. As demonstrated in Fig. 9, two open shrinkage cavities are present in Sample 2. The results from the XCT analysis confirm the presence of sealant resin in one of the pores, the smaller one, but not in the larger one, as depicted in Fig. 9(b). The presence of the sealant material within the smaller cavity is additionally confirmed by examining the variation in grey values of the pixels across both open shrinkage cavities, as illustrated in Fig. 10. The plotted grey value changes clearly emphasize the difference between the two cavities with the sealed cavity's pixel value hovering around 70. In contrast, the unsealed cavity's value remains close to zero. Since the plotted diagram indicates an average grey value of approximately 150 for the Al alloy material, it can be affirmed that the material present within the sealed smaller cavity is the polymer resin used.

The Sample 3 exhibits a moderate leak compared to the other two samples; however, it shows a complete absence of leakage after being subjected to the VPI with the Super Sealant resin. Micro XCT results reveal intriguing insights into the sealing condition of the primary leakage path, as demonstrated by the 3D CT visualized in Fig. 11.

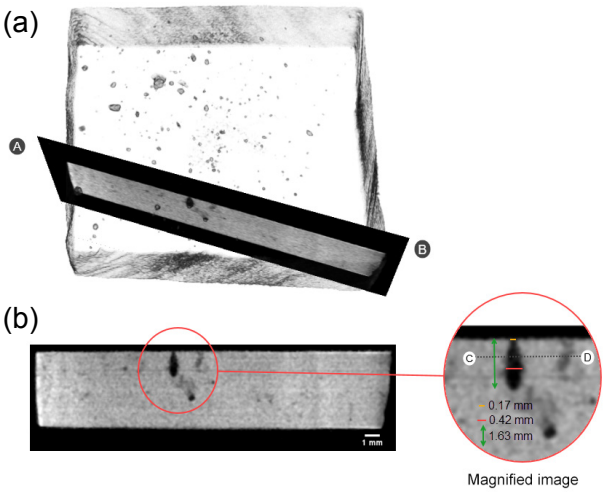

Fig. 9: CT images of Sample 2: (a) 3D CT image; (b) CT slice image across the Line AB

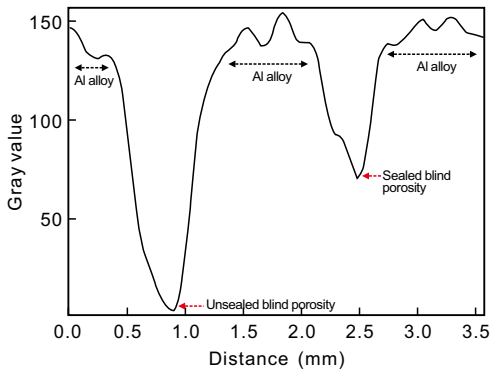

Fig. 10: Pixel's gray values plotting across the Line CD in the magnified image of Fig. 9(b)

The primary leakage path is found to be non-uniform and not aligned. A substantial internal casting cavity was observed in the sample, as demonstrated in various side views in Fig. 11. It can be noticed that the disappearance of the leakage path in a region, as highlighted by red circles in the 3D CT images, offers valuable insight into the presence of the sealant material. 2D CT slice images were analyzed over the disappearance region to further investigate and identify evidence of the resin's existence. The cross-sectional CT slice image of the leakage reveals that the impregnating resin can not seal the entire path but is only located in the above narrow region of the leakage path, as shown in Fig. 12(b). The cavity opening size at the top and bottom of the leakage path is measured to be approximately 0.31 mm and 0.55 mm, respectively, as indicated in the magnified image in Fig. 12(b). The magnified CT image also shows that the cavity of the leakage path has expanded to approximately 2.18 mm within the sample. The presence of the sealant material is found to be limited, with a size ranging from around 0.04 mm to 0.15 mm.

Due to limited grey value contrast, it is challenging to identify the impregnating resin in a small region of the leakage path. To confirm the presence of the resin sealant in Sample 3, further CT slice image analysis of the leakage was conducted, as shown in Fig. 13.

Figure 13(a) shows the 2D CT image along Line AB in Fig. 13(1). The central crack appears as a black region, lacking the impregnating material. However, grey variations indicate the presence of sealant resin in more minor branching defects stemming from noticeable cracks in Al alloy Sample 3. In the 2D CT image along the Line CD of the 3D CT [Fig. 13(b)], no sealant resin is observed, confirming the reduced size of the leakage path. Figure 13(c) confirms the presence of impregnating resin in a confined area of the leakage, aligning with the findings in Fig. 12. The slice image in Fig. 13(d) reveals the absence of sealant material at the bottom of the leakage path. The presence of ring artifacts in the 2D CT images slightly impacts the qualitative analysis of the resin.

Figure 14(c) shows a fully enclosed pore near the surface of Sample 3. These defects cannot be sealed directly through the impregnation but can become exposed to the atmosphere after machining, leading to product failure. Therefore, performing impregnation on machined die-cast Al alloys is crucial to strengthen them and prevent issues like corrosion. An open shrinkage cavity resulting from the HPDC is effectively sealed in the VPI, as presented in Fig. 14(d). Although the impregnated polymer resin in the casting defects was qualitatively identified based on grey contrast in the CT images, a quantitative method is necessary to confirm the resin as the P601 Super Sealant.

3.3 Quantitative micro-CT analysis

Identifying low atomic number impregnation material within the A383 alloy defects as the Super Sealant P601 was conducted using the DXCT method on Sample 3. To accomplish this, the photon-counting XCounter detector was employed, with a layout of 2048×64 pixels, one-fourth the

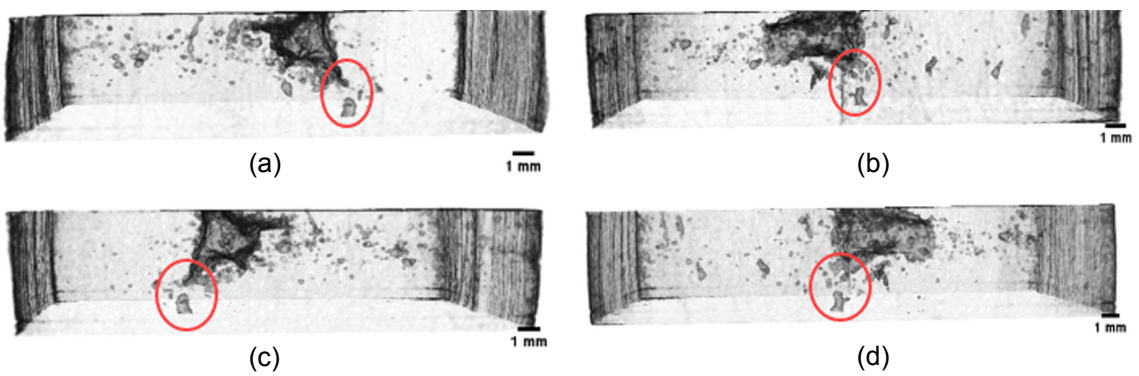

Fig. 11: 3D CT images of Sample 3: (a), (b), (c), and (d) side views, respectively, by clock-wise rotation of the sample

width of the FPD used in the qualitative investigation. Given our specific interest in the ROI within the alloy sample for DXCT, the fan-beam geometry of the X-ray source was utilized. The fan-beam configuration involves a narrow, fan-shaped X-ray beam that covers an object's specific section or slice. This approach ensures that the CT images exhibit high clarity and uniformity, enabling precise identification of the impregnation resin within the internal casting defects. Thus, the inspection area was selected with the utmost care, using a 2.3 maximum geometrical magnification of the alloy sample. The inner structure of the selected section of Sample 3 in the DXCT is visualized in 3D CT form in Fig. 15(a). The areas for calculating EANs for the Al alloy and impregnated resin were considered, as depicted in the 2D CT slice image in Fig. 15(b). The average linear attenuation coefficients for the low and high-energy windows CT images, shown in Figs. 15(c) and (d), were used to calculate the EANs based on Eq. (2).

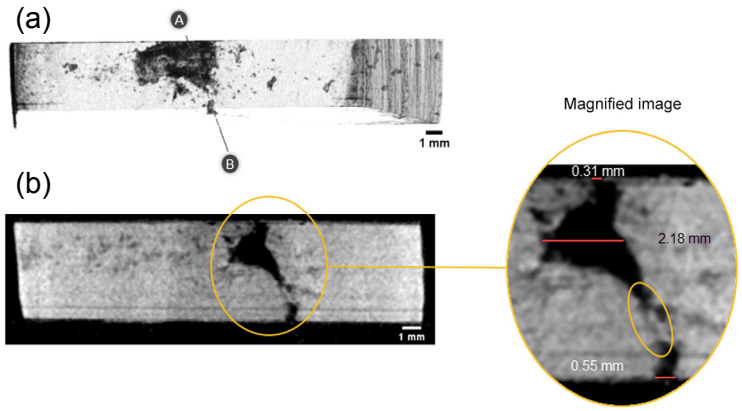

Fig. 12: CT images of Sample 3: (a) 3D CT image; (b) CT slice across the Line AB of the 3D image

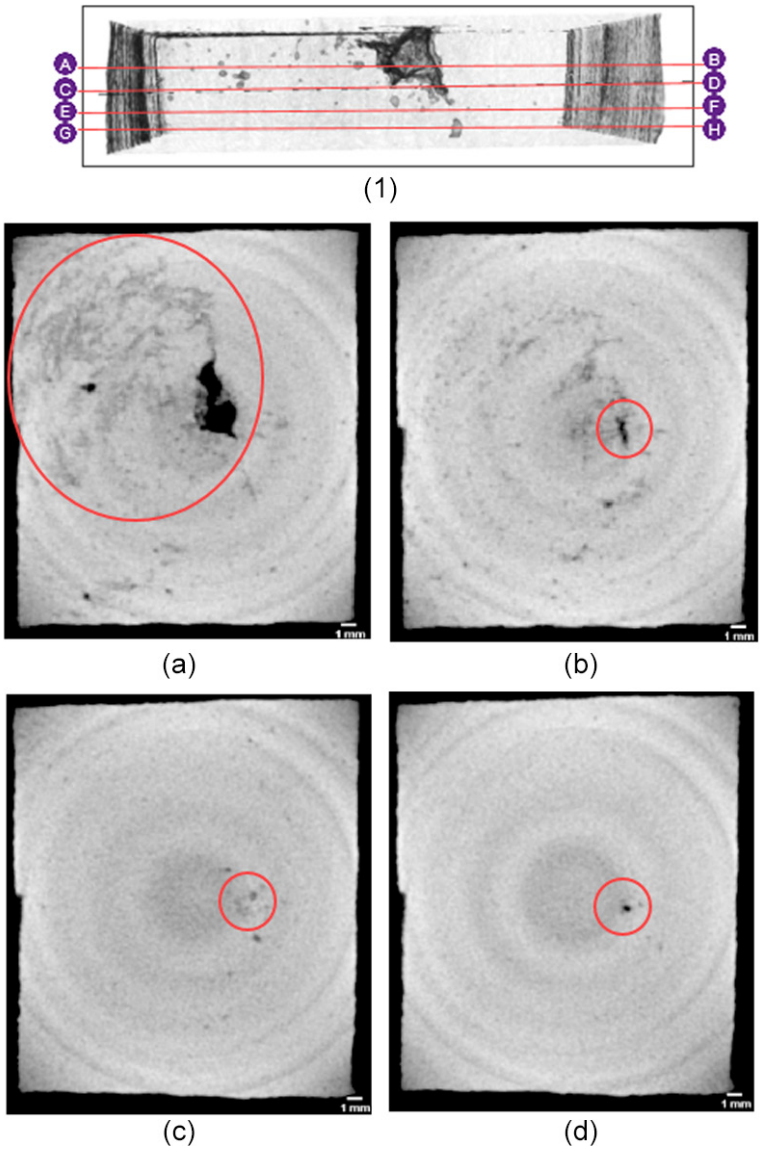

Fig. 13: CT images of Sample 3: (1) 3D CT images; (a–d) CT slice images across the Lines AB (a), CD (b), EF (c) and GH (d) of the 3D images

The selected region for analysis was located near the middle of Sample 3, a comparatively large crack in the leakage path can be observed, which is visible in black as the impregnated sealant has not sealed it. Due to its lower X-ray attenuation, the impregnated material in the casting defects of the sample appears in a low grey color contrast compared to the ADC12 parts. The linear attenuation coefficient values and computed EANs for both regions are presented in Table 2. The higher linear attenuation coefficients for the Al alloys and impregnated parts in the low-energy (30–50 keV) range could be observed compared to the higher-energy (70–90 keV) windows. The Al alloy region demonstrates more significant X-ray photon attenuation due to its comparatively higher atomic number and density, leading to more photoelectric interactions. The reduced linear attenuation in the higher-energy windows results from decreased total X-ray attenuation through photoelectric and Compton scatterings. Although Compton scattering becomes the predominant cause of attenuation in the higher energy region, it does not significantly impact the attenuation of the Al alloys, which possess a higher atomic number, as both the alloys and the impregnated materials show around similar values in this study.

The experimental EANs ($Z_{eff(exp)}$) of the impregnated material and the Al alloys in Sample 3 were compared with their theoretically computed EANs ($Z_{eff(th)}$). The $Z_{eff(th)}$ of the P601 polymer resin was determined using the XMuDat program, which considered hydroxyl ethyl methacrylate as the sole constituent. However, it is known that P601 is a complex mixture of various chemical compounds, including methacrylate monomers, initiators, and inhibitors. In addition, A383

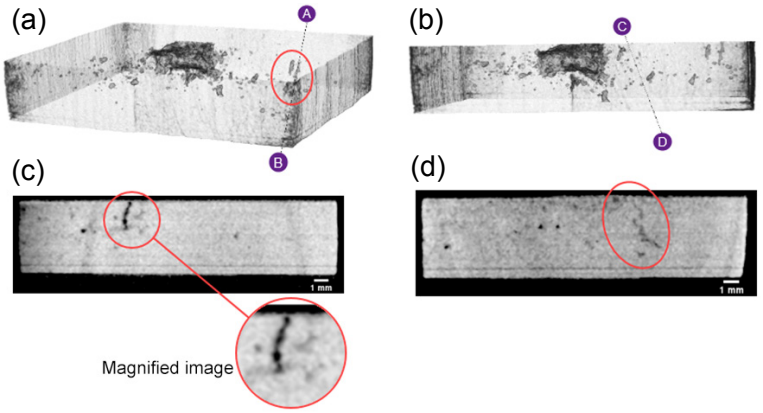

Fig. 14: CT images of Sample 3: (a, b) 3D CT images; (c, d) cross-sectional CT images across the Lines AB (a) and CD (d) of 3D CT images

Al alloy is composed of a eutectic mixture of elements such as Si, Cu, Ti, Mn, V, and Cr. For this study, the atomic number of Al is considered as the $Z_{eff(th)}$ of the Al alloys, as depicted in Table 2. As a result, a deviation of 4.79% and 5.31% is observed in the $Z_{eff(exp)}$ values for P601 and Al alloys, respectively.

The variations in EANs can be effectively visualized using graphical representations, as illustrated in Fig. 16. The vertical bar charts demonstrate a close correlation between the calculated $Z_{eff(exp)}$ of the impregnated resin in the die-casting defects of Sample 3 and the $Z_{eff(th)}$ of the P601 resin, as shown in Fig. 16(a).

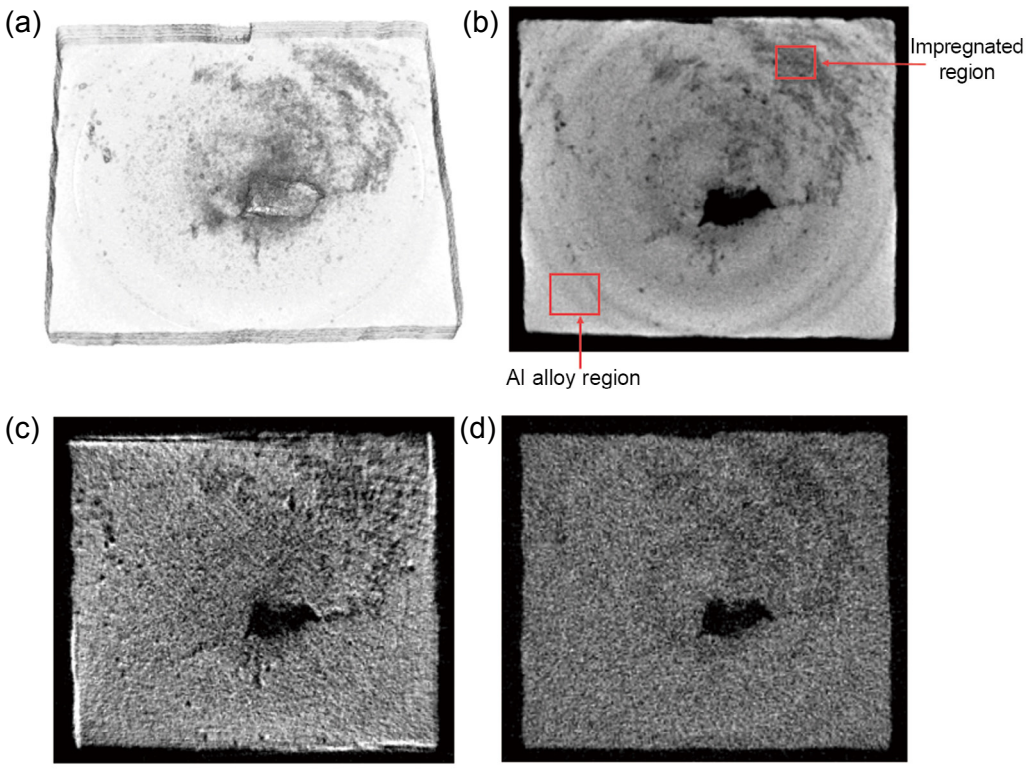

Fig. 15: DXCT of Sample 3: (a) 3D CT image; (b) total-energy 2D CT; (c) low-energy 2D CT; (d) high-energy 2D CT

Table 2: Comparation of experimental and theoretical effective atomic numbers in Al alloys and P601 polymer resin

	μ (E_1) (30–50 keV) (Average)	μ (E_2) (70–90 keV) (Average)	$Z_{eff(exp)}$	$\frac{(Z_{eff(exp)}-Z_{eff(th)})}{Z_{eff(th)}}$
Impregnated region ($Z_{eff(th)}$ of P601=7.09)	$3.92\times10^{+11}$	$2.87\times10^{+11}$	6.75	–4.79%
Al alloy region ($Z_{eff(th)}$ of Al=13)	$7.79\times10^{+11}$	$2.53\times10^{+11}$	13.69	5.31%

Additionally, a significant distinction is observed between the $Z_{eff(exp)}$ of the impregnated region and the Al alloy region, as depicted in Fig. 16(b). This result demonstrates that the DXCT technique can effectively be used to quantitatively identify low atomic number resin used in the impregnation for sealing internal casting defects in metal alloys, unlike the conventional leak test. Thus, micro XCT provides a nondestructive and versatile approach to comprehensively evaluate the efficacy of impregnation treatments in sealing die-casting defects in industrial metals.

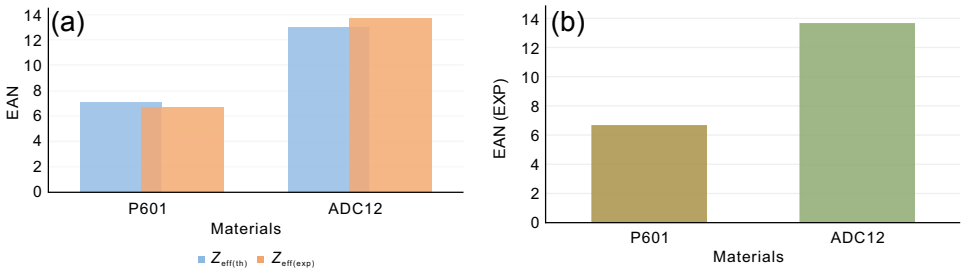

Fig. 16: Effective atomic numbers comparison of the P601 and the ADC12 of Sample 3: (a) $Z_{eff(th)}$ and $Z_{eff(exp)}$ comparison of the P601 and ADC12; (b) $Z_{eff(exp)}$ comparison of the P601 and ADC12

4 Conclusion

The evaluation of the VPI technique's efficacy in sealing Al alloy die-casting defects was comprehensively studied using advanced direct conversion X-ray FPDs coupled with a laboratory-based semi-automated micro XCT. The study findings reveal that relying solely on dipping water leak tests to assess the sealing performance of alloy leakage paths, as per industrial standards, is unreliable. Micro XCT provides nondestructive insights, revealing more significant details. The qualitative analysis with micro XCT enables visualization of the internal structures of the Al alloy samples in 3D CT images, exposing non-uniform and non-linear leakage paths contrary to assumptions from the leak test. The significant cracks are observed in the middle of the primary leakage paths of Samples 1 and 3. The low atomic number impregnation resin sealant in the internal casting defects of the alloy samples is successfully exhibited using the grey color contrast in 2D CT images. The zero leakage noticed in the leak test of Sample 2 after the VPI treatment is also confirmed in the CT analysis. However, CT cross-sectional images reveal the absence of resin material at the initial points of the leakage path. This investigation also unveils open shrinkage cavities, with Sample 2 exhibiting a comparatively large open cavity without the sealant. Despite zero leakage in the leak test, micro XCT results indicate incomplete airtight sealing in Sample 3, confined to a narrow region along the primary leakage path. The XCT examination also detects fully enclosed pores near the surface of Sample 3, which requires impregnation after machining. Quantitative identification of impregnated sealant resin in Al alloy defects using DXCT reveals that the EAN corresponding to the P601 Super Sealant resin deviates by 4.79% from its theoretical value. This findings emphasize the importance of utilizing X-ray CT to evaluate the sealing efficacy of impregnated die-casting metals, highlighting the inadequacy of relying solely on leak tests. The study's results can be considered for optimizing the standard VPI process parameters and impregnation sealant properties to ensure high-quality sealing of industrial metal products.

Acknowledgment

The authors would like to extend their appreciation to the members of ANSeeN Inc. for their technical and instrument support to the XCT.

Conflict of interest

The authors declare that they have no conflicts of interest related to this research.

References

[1] Czerwinski F. Current trends in automotive lightweighting strategies and materials. Materials, 2021, 14(21): 6631. https://doi.org/10.3390/ma14216631
[2] Relland J, Bax L, Ierdes M A. Vision on the future of automotive lightweighting. Alliance: Surrey, UK, 2019.
[3] Campbell F C. Lightweight materials: Understanding the basics. ASM International: Materials Park, Ohio, USA, 2012.
[4] Hirsch J, Al-Samman T. Superior light metals by texture engineering: Optimized aluminum and magnesium alloys for automotive applications. Acta Materialia, 2013, 61(3): 818–843.
[5] Joost W J, Krajewski P E. Towards magnesium alloys for high-volume automotive applications. Scripta Materialia, 2017, 128: 107–12.
[6] Liu D F, Tao J. Application of automobile lightweight alloys and the development of its die-casting technology. Advanced Materials Research, 2011, 308–310: 785–789. https://doi.org/10.4028/www.scientific.net/AMR.308-310.785
[7] Bonollo F, Gramegna N, Timelli G. High-pressure die-casting: Contradictions and challenges. JOM, 2015, 67: 901–908. https://doi.org/10.1007/s11837-015-1333-8
[8] Luo A A, Sachdev A K, Apelian D. Alloy development and process innovations for light metals casting. Journal of Materials Processing Technology, 2022, 306: 117606.
[9] Walkington W G. Die casting defects–Causes and solutions. 1st ed., Des Plaines, IL: North American Die Casting Association, 2003: 1–11.
[10] Fioreseb E, Bonollo F, Timelli G, et al. New classification of defects and imperfections for aluminum alloy castings. Int. J. Met., 2015, 9(1): 55–66. https://doi.org/10.1007/BF03355602
[11] Andresen B. Die casting engineering: A hydraulic, thermal, and mechanical process. Marcel Dekker, New York, 2005.
[12] NADCA product specification standards for die casting. Publication #402, 10th edn. Arlington Heights, IL: North American Die Casting Association, 2018.
[13] Twarog D. State of the die casting industry. Die Casting Engineer, 2005, 49(1): 16–18.
[14] Blondheim D, Monroe A. Macro porosity formation: A study in high pressure die casting. International Journal of Metalcasting, 2022, 16: 330–341. https://doi.org/10.1007/s40962-021-00602-x
[15] Blondheim D. Improving manufacturing applications of machine learning by understanding defect classification and the critical error threshold. International Journal of Metalcasting, 2022, 16: 502–520. https://doi.org/10.1007/s40962-021-00637-0
[16] Lattanzi L, Fabrizi A, Fortini A, et al. Effects of microstructure and casting defects on the fatigue behavior of the high-pressure die-cast AlSi9Cu3(Fe) alloy. Procedia Structural Integrity, 2017, 7: 505–512. https://doi.org/10.1016/j.prostr.2017.11.119

[17] Bonollo F, Urban J, Bonatto B, et al. Gravity and low pressure die casting of aluminium alloys: A technical and economical benchmark. La Metallurgia Italiana, 2005, 97: 23–32.
[18] Timelli G and Bonollo F. Quality mapping of aluminium alloy diecastings. Metall. Sci. Technol., 2008, 26(1): 2–8.
[19] Iwata Y, Dong S, Sugiyama Y, et al. Effects of solidification behavior during filling on surface defects of aluminum alloy die casting. Materials Transactions, 2013, 54(10): 1944–1950.
[20] Trometer N, Godlewski L A, Prabhu E, et al. Effect of vacuum on die filling in high pressure die casting: Water analog, process simulation and casting validation. International Journal of Metalcasting, 2024, 18: 69–85. https://doi.org/10.1007/s40962-023-01002-z
[21] Nunes H, Emadinia O, Vieira M F, et al. Low- and high-pressure casting aluminum alloys: A review. In Recent Advancements in Aluminum Alloys; IntechOpen: London, UK, 2023. Available online: https://www.intechopen.com/online-first/85913 (accessed on 30 December 2023)
[22] Wilczek A, Długosz P, Hebda M. Porosity characterization of aluminium castings by using particular non-destructive techniques. Journal of Nondestructive Evaluation, 2015, 34(3): 1–7. https://doi.org/10.1007/s10921-015-0302-z
[23] Niu X P, Hu B H, Pinwill I, et al. Vacuum assisted high pressure die casting of aluminium alloys. Journal of Materials Processing Technology, 2000, 105(1–2): 119–127.
[24] Shi X Y, Li D J, Luo A A, et al. Microstructure and mechanical properties of Mg-7Al-2Sn alloy processed by super vacuum die-casting. Metallurgical and Materials Transactions: A, 2013, 44: 4788–4799.
[25] Yu W B, Yuan Z H, Guo Z P, et al. Characterization of A390 aluminum alloy produced at different slow shot speeds using vacuum assisted high pressure die casting. Transactions of Nonferrous Metals Society of China, 2017, 27(12): 2529–2538.
[26] Cao H X, Hao M Y, Shen C, et al. The influence of different vacuum degree on the porosity and mechanical properties of aluminum die casting. Vacuum, 2017, 146: 278–281.
[27] Dong X X, Zhu X Z, Ji S X. Effect of super vacuum assisted high pressure die casting on the repeatability of mechanical properties of Al-Si-Mg-Mn die-cast alloys. Journal of Materials Processing Technology, 2019, 266: 105–113.
[28] Wen Wei, Luo A A, Zhai T G, et al. Improved bending fatigue and corrosion properties of a Mg-Al-Mn alloy by super vacuum die casting. Scripta Materialia, 2012, 67(11): 879–882.
[29] Hu C, Zhao H D, Wang X L, et al. Microstructure and properties of AlSi12Fe alloy high pressure die-castings under different vacuum levels. Vacuum, 2020, 180: 109561.
[30] Szalva P, Orbulov I N. The effect of vacuum on the mechanical properties of die cast aluminum AlSi9Cu3(Fe) alloy. International Journal of Metalcasting, 2019, 13: 853–864. https://doi.org/10.1007/s40962-018-00302-z
[31] Mathew J, Williams M A, Srirangam P. X-ray computed tomography studies on porosity distribution in vacuum induction cast Al-7Si alloys. JOM, 2021, 73: 3866–3872. https://doi.org/10.1007/s11837-021-04944-z
[32] Kan K, Imura Y, Morii H, et al. Application of photon-counting X-ray computed tomography to aluminum-casting inspection. World Journal of Nuclear Science and Technology, 2013, 3(3): 106–108.
[33] Bandara A, Kan K, Morii H, et al. X-ray computed tomography to investigate industrial cast Al-alloys. Production Engineering, 2019, 14: 147–156. https://doi.org/10.1007/s11740-019-00946-8.2019.12.20
[34] Soga N, Bandara A, Kan K, et al. Micro-computed tomography to analyze industrial die-cast Al-alloys and examine impregnation polymer resin as a casting cavity sealant. Production Engineering, 2021, 15(6): 885–896.
[35] Yusuke K, Bandara A, Soga N, et al. Investigation of industrial die-cast Al-alloys using X-ray micro-computed tomography and machine learning approach for CT segmentation. Production Engineering, 2023, 17(2): 291–305.
[36] Impregnation of porous metal casting and powdered metal components. US, Military Standard, MIL STD 276A, 1992.
[37] Du Plessis A, Rossouw P. X-ray computed tomography of a titanium aerospace investment casting. Case Studies in Nondestructive Testing and Evaluation, 2015. https://doi.org/10.1016/j.csndt.2015.03.001
[38] Kastner J, Harrer B, Degischer H P. High resolution cone beam X-ray computed tomography of 3D-microstructures of cast Al-alloys. Materials Characterization, 2011, 62(1): 99–107.
[39] Hellier C J. Handbook of nondestructive evaluation, 2nd edn. McGraw-Hill, Columbus, 2013.
[40] Garcea S C, Wang Y, Withers P J. X-ray computed tomography of polymer composites. Composites Science and Technology, 2018, 156: 305–319.
[41] Buratti A, Bredemann J, Pavan M, et al. Applications of CT for dimensional metrology. In: Carmignato S, Dewulf W, Leach R (eds.), Industrial X-ray Computed Tomography, Springer, Cham., 2018: 333–369.
[42] Kastner J, Heinzl C. X-ray computed tomography for nondestructive testing and materials characterization. In: Liu Z, Ukida H, Ramuhalli P, Niel K (eds.), Integrated Imaging and Vision Techniques for Industrial Inspection. Springer, London, 2015: 227–250.
[43] Reinhart C. Industrial computer tomography-A universal inspection tool. In: 17th World Conference on Nondestructive Testing, Shanghai, China, 25-28 Oct. 2008.
[44] Thompson A, Leach R. Introduction to industrial X-ray computed tomography. In: Carmignato S, Dewulf W, Leach R (eds.), Industrial X-ray Computed Tomography, Springer, Cham., 2018: 1–23.
[45] Hanke R, Theobald F, Norman U. X-ray based methods for non-destructive testing and material characterization. Nuclear Instruments and Methods in Physics Research Section A: Accelerators, Spectrometers, Detectors and Associated Equipment, 2008, 591(1): 14–18.
[46] Ohno Y, Torikoshi M, Tsunoo T, et al. Dual-energy X-ray CT with CdTe array and its extension. Nucl. Instrum. Methods Phys. Res. A, 2005, 548(1–2): 72–77. https://doi.org/10.1016/j.nima.2005.03.069
[47] Torikoshi M, Tsunoo T, Endo M, et al. Design of synchrotron light source and its beamline dedicated to dual-energy X-ray computed tomography. Journal of Biomedical Optics, 2001, 6(3): 371–377.
[48] Kim H, Yoseop H, and Jaikoo P. Evaluation of permeable pore sizes of macroporous materials using a modified gas permeation method. Materials Characterization, 2009, 60(1): 14–20.
[49] Muders J, Hesser J, Lachner A, et al. Accuracy evaluation and exploration of measurement uncertainty for exact helical cone beam reconstruction using katsevich fltered back projection in comparison to circular Feldkamp reconstruction with respect to industrial CT metrology. In: International Symposium on Digital Industrial Radiology and Computed Tomography, Berlin, Germany, 2011.
[50] Kyrieleis A, Titarenko V, Ibison M, et al. Region-ofnterest tomography using fltered backprojection: Assessing the practical limits. J. Microsc., 2010, 241: 69–82.
[51] Kikinis R, Pieper S D, Vosburgh K. 3D slicer: A platform for subject-specifc image analysis, visualization, and clinical support. In: Jolesz FA (ed.), Intraoperative Imaging Image-Guided Therapy, 2014, 3(19): 277–289.
[52] Schindelin J, Arganda-Carreras I, Frise E, et al. Fiji: An open-source platform for biological-image analysis. Nature Methods, 2012, 9: 676–682. https://doi.org/10.1038/nmeth.2019
[53] de Oliveira F B, Stolf A, Bartscher M, et al. Experimental investigation of surface determination process on multi-material components for dimensional computed tomography. Case Studies in Nondestructive Testing and Evaluation, 2016, 6B: 93–103. https://doi.org/10.1016/j.csndt.2016.04.003
[54] Jackson D F, Hawkes D J. X-ray attenuation coefcients of elements and mixtures. Phys. Rep., 1981, 70(3): 169–233.
[55] Hawkes D J, Jackson D F. An accurate parametrisation of the X-ray attenuation coefcient. Phys. Med. Biol., 1980, 25(6): 1167–1171.
[56] Nowotny R. XMuDat: Photon attenuation data on PC. IAEA-NDS-195 International Atomic Energy Agency, Vienna, Austria, 1998.